nature communications

Article

https://doi.org/10.1038/s41467-026-68426-z

Phase-controlled growth of 2D crystals of the MB_2T_4 family via a flux-assisted method

Received: 14 January 2025

Accepted: 7 January 2026

Published online: 14 January 2026

Check for updates

Xingguo Wang[1,2,3,4,8], Shiqi Yang[5,8], Xinyue Huang[5], Juntian Wei[3], Huaning Jiang[3], Qianqian He[3,6], Kunpeng Si[1,3], Bixuan Li[1,3], Yu Ye[5], Beng Kang Tay[2,7], Peng Zhang[1,3] ✉, Zheng Liu[4] ✉ & Yongji Gong[1,3] ✉

Van der Waals materials of the MB_2T_4 family (M = transition metal or rare-earth metal, B = Bi or Sb, T = Te, Se, or S) have attracted wide interest for their exotic topological and magnetic properties, as well as potential spintronic applications. However, the direct growth of 2D ternary MB_2T_4 remains challenging due to multiple competing phases and complex atomic arrangements. Here, we report a flux-assisted, phase-controlled growth strategy to directly grow six distinct 2D MB_2T_4 crystals. Using MB_2T_4 bulk powder as precursor, its dissolution into the cosolvent ensures stoichiometric control, while thermodynamic-kinetic equilibrium suppresses phase separation. Taking $MnSb_2Te_4$ as an example, we obtained highly ordered septuple layers, with superconducting quantum interference device (SQUID) and reflective magnetic circular dichroism (RMCD) measurements confirming layer-dependent ferromagnetism and Curie temperature (T_c) ranging from 12.3 to 33.7 K. This strategy provides an effective route for synthesizing complex layered crystals and offers versatile platforms for advancing spintronic applications.

With the pursuit of understanding and researching certain fundamental physical topics, such as quantum anomalous Hall effect[1], axion electrodynamics[2], topological conductivity[3], and Majorana fermions[2,4], tremendous efforts have been devoted to exploring suitable materials platforms theoretically and experimentally[1,3,5–9]. Recently, a new kind of van der Waals layered MB_2T_4 family materials has acquired considerable attention due to their exotic properties containing topological electronic states and (anti)ferromagnetism simultaneously[2,7,10–13]. Specifically, layer-dependent magnetic behaviors have been predicted and observed in $MnBi_2Te_4$ single crystals, where odd-layer samples indicate uncompensated ferromagnetic properties while even-layer crystals display antiferromagnetic features below 25 K[14]. Besides, both theoretical simulation and angle-resolved photoemission spectroscopy (ARPES) results show that the electronic structure of specific members of MB_2T_4 family materials, such as $MnSb_2Te_4$ and $MnBi_2Te_4$, possesses the surface Dirac cone structure, showing their promising potential for topological research and applications[1,5,15]. For instance, it is reported that a large magnetic gap of up to 90 meV at 1 K has been observed in $MnBi_4Te_7$, which is significantly enhanced by a self-organized alternating sequence of $MnBi_2Te_4$ septuple layers (SL) and Bi_2Te_3 quintuple layers (QL)[1], inspiring the design of devices to achieve dissipation-less transport in the future[16,17].

Despite the superior and attractive properties of the MB_2T_4 family, the direct preparation of their ultrathin single-crystal flakes is still restricted due to their complex septuple-atom structures, varieties of phases, and strong interlayer van der Waals forces[18–20]. Recent attempts to obtain several-layer MB_2T_4 family samples only rely on Au-assisted exfoliation, Al_2O_3-assisted exfoliation, and molecular beam

[1]Tianmushan Laboratory, Beihang University, Hangzhou, China. [2]CNRS-International-NTU-Thales Research Alliance, Nanyang Technological University, Singapore, Singapore. [3]School of Materials Science and Engineering, Beihang University, Beijing, China. [4]School of Materials Science and Engineering, Nanyang Technological University, Singapore, Singapore. [5]State Key Laboratory for Mesoscopic Physics and Frontiers Science Center for Nano-optoelectronics, School of Physics, Peking University, Beijing, China. [6]The Analysis & Testing Center, Beihang University, Beijing, China. [7]School of Electrical and Electronic Engineering, Nanyang Technological University, Singapore, Singapore. [8]These authors contributed equally: Xingguo Wang, Shiqi Yang.
✉e-mail: x_l_zhang@buaa.edu.cn; z.liu@ntu.edu.sg; yongjigong@buaa.edu.cn

epitaxy (MBE)[10,19,21–28]. Other methods, such as evaporation-rate-controlled chemical vapor deposition (CVD), have been adapted to grow multilayered $MnBi_2Te_4$ and $MnBi_4Te_7$. However, due to the difficulty in controlling precursor distribution, thermodynamics, and kinetics, the effective phase-controlled growth routes and patterns of these MB_2T_4 family materials are still not fully understood, which restricts the widespread exploration and application[29].

Herein, we developed the flux-assisted phase-controlled growth method to obtain $MnSb_2Te_4$ nanosheets directly. $MnSb_2Te_4$ powder is directly utilized as precursors to be dissolved into the NaCl and KCl mixture flux, ensuring the stoichiometry ratio and uniform distribution. Then reaction thermodynamics and kinetics are regulated by temperature, together with the ratio of flux. An in-situ heating experiment and energy dispersive X-ray spectroscopy (EDS) mapping analysis prove the mechanism of crystallization. The thickness of $MnSb_2Te_4$ nanosheets can be adjusted to as thin as 2.4 nm, and the lateral size is tens of microns. Then aberration-corrected transmission electron microscope (AC-TEM) images show the crystal structure with SL-atom arrangement, indicating the capability of the phase control in 2D $MnSb_2Te_4$. Other 2D MB_2T_4 family crystals, including $MnSb_4Te_7$, $MnBi_2Te_4$, $MnBi_4Te_7$, $MnBi_2Se_4$, and $MnBi_4Se_7$, can be obtained via a similar strategy, which provides promising platforms to investigate their magnetic properties and applications.

Results and discussion

Flux-assisted growth strategy and process

The growth process and phase control are shown in Fig. 1a. First, $MnSb_2Te_4$ powder is synthesized and then tested by EDS in Supplementary Fig. 1. Then, a mixture of 1:1 molar ratio of KCl and NaCl as cosolvent with $MnSb_2Te_4$ powder is placed between two pieces of mica[30]. Next, these mica are tightly pressed between the self-designed setup, which consists of two 304 stainless steel plates (10 cm in length, 2 cm in width, and 0.3 cm in thickness). Screw holes are machined into the plates to allow for mechanical fastening. When all screws are fully tightened, the setup can generate a pressure of about 1.7×10^5 Pa, as measured by the thin-film sensor in Supplementary Fig. 3. However, due to the size of the precursor and cosolvent particles, the stacked mica cannot achieve perfect nanoscale contact, leaving the confined space partially open. After loading it into a tube furnace, the setup was heated under a continuous Ar flow. When the temperature goes up to 650 °C, the mixed salts gradually melt into a liquid state to dissolve the precursor powder stoichiometrically. It can almost maintain a stable and evenly distributed atomic ratio compared with the traditional methods, which provide the primary conditions for phase control. Molten flux may be squeezed out, and any volatile species formed inside can escape with the carrier Ar gas through the mica edges. Then the acquisition of the target phase can be achieved through careful temperature control. Notably, at high temperatures over 760 °C, $MnSb_2Te_4$ powder is quite easy to decompose and separate into Sb_2Te_3 and MnTe phases. In contrast, when the synthesis temperature is below the melting temperature of the flux mixture, no obvious reaction occurs. The melting point of the mixed salt of equimolar KCl and NaCl is ~650 °C according to the differential scanning calorimeter (DSC) result in Fig. 1b. Additionally, it is found that the endothermic peaks around the red region for the mixture of flux and precursors (mass ratio of 2:1) are similar to that for the NaCl–KCl flux, indicating the fact that the melting of the flux and the dissolution of the precursor are nearly simultaneous. Besides, nine kinds of fluxes with different melting points have been applied and listed in Fig. 1c, where the cyan region indicates that the temperature is too high to prevent the phase separation. As for the flux candidates located in the blue region, such as NaI, NaI–KCl, and LiCl, together with KI, are prone to inducing deliquescence reactions easily in the air, leading to the growth of antimony oxyhalides[31]. $MnCl_2$ and Te in the red part may provide an excess of Mn or Te sources, which goes against the composition control. Consequently, the cosolvent of NaCl–KCl with a proper melting point and good chemical inertness is the best choice for synthesizing $MnSb_2Te_4$ nanocrystals.

Figures 1d, e reveal the evolution of the chemical composition and reaction process with growth temperature, respectively, further elaborating on the mechanism of temperature in phase control. All the statistical data in Fig. 1d are collected from the EDS results of 156 triangular or hexagonal samples. It is obvious that maximum yield with the stoichiometric ratio ~1:2 of Mn: Sb can be obtained at 700 °C. According to the $MnSb_2Te_4$ phase diagram, 647 °C is the formation temperature for $MnSb_2Te_4$[32]. However, when the flux begins to melt at ~650 °C, only a tiny fraction of precursor powder dissolves into the molten flux mixture, which reduces the probability of three types of precursor atoms encountering each other compared with the meeting of two kinds of atoms, resulting in the nucleation of bi-element compounds and phase separation. At this range, the thermodynamics of the target reaction are favorable, and the main factor leading to phase separation is the lack of compatibility in kinetics, as shown in the blue part in Fig. 1e. With the temperature rising to 700 °C, the dissolved precursor atoms dramatically increase and tend to crystallize into the target nanosheets, exhibiting both thermodynamic and kinetic compatibility. Once the growth temperature is higher than 730 °C, the reaction paths are dominated by temperature rather than the diffusion of reactant atoms, promoting the generation of thermodynamically stable Sb_2Te_3 and MnTe phases, as shown in the red part in Fig. 1e.

As for the thickness of the obtained samples, synthesis temperature, and the ratio of cosolvents/precursors play a crucial role, as shown in Supplementary Fig. 7. It is found that the minimum thickness detected by AFM increases with the synthesis temperature rising, which may be attributed to the increased concentration of the dissolved precursors in flux at high temperatures, leading to thermodynamically rapid vertical crystallization, which shows similar trend to the previous discussion[31]. Besides, the thickness can also be effectively tuned by the ratio of cosolvents and precursors. It is found that thinner samples can usually be formed when the percentage of precursors decreases. This is because in such a situation, there are insufficient atoms available to facilitate both lateral and vertical expansion[31], causing small and thinner samples. Figure 1f shows the typical morphology of the obtained nanosheets in a large view, where the lateral size of the samples can be up to tens of microns. More optical images with different thicknesses are shown in Supplementary Figs. 8, 9, and 10. The minimum thickness for $MnSb_2Te_4$ is 2.4 nm in Fig. 1g, equivalent to the 2-layer thickness, with the inset showing the corresponding height profile. EDS mapping over a ~450 μm region in Fig. 1h shows elemental distributions of different nanosheets. Histogram in Fig. 1i displays the Mn:Sb ratios for 44 samples grown at 700 °C, where ~72.7% are close to the ideal 1:2 stoichiometry, while the remainder likely corresponds to phase-separation products.

Phase-control mechanism and universality

To better reveal the mechanism of the flux-assisted precipitation process, in-situ heating experiments were designed and conducted with the optical microscope as an observation and recording medium shown in Fig. 2a. Supplementary Movie 1 and optical images in Supplementary Fig. 13 record every step of the melting and precipitation process. Besides, ex-situ SEM obtained at 500, 700, and 760 °C is used to verify the chemical species at each step. First, below the melting point of the flux, all precursors and flux maintain a solid state. Then, as the temperature is increased to 650 °C, flux powder begins to melt into fluid and flow easily on the substrate. Meanwhile, the precursors dissolve into the liquid cosolvents to form the final flux mixture, as shown in Supplementary Fig. 17. With the volatilization of the cosolvent, the oversaturated flux will generate ultrathin $MnSb_2Te_4$ crystals. The main products generated at 700 °C are $MnSb_2Te_4$ single crystals. If the temperature continuously goes up, $MnSb_2Te_4$ flakes will further

https://doi.org/10.1038/s41467-026-68426-z

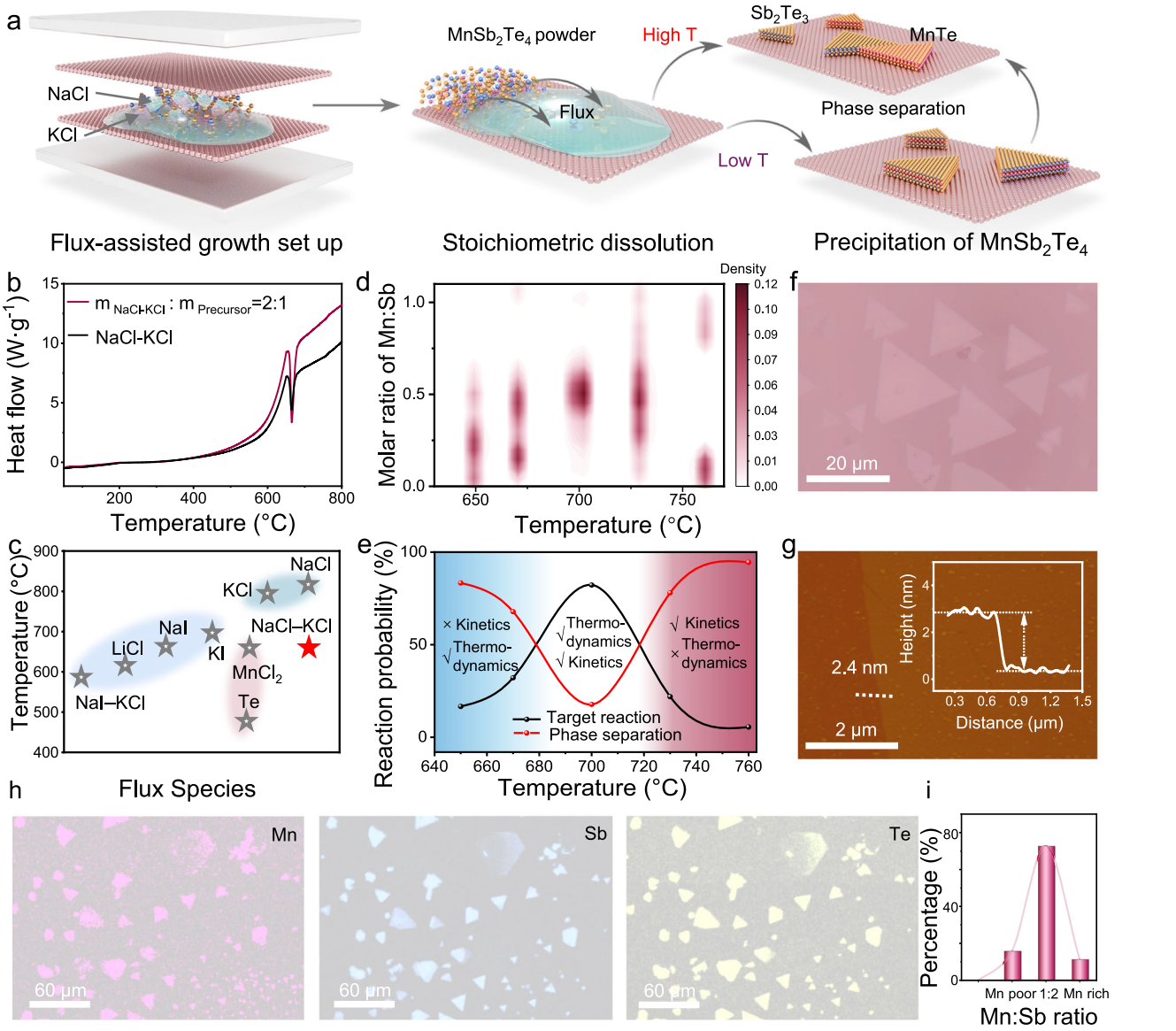

Fig. 1 | Synthesis scheme and characterizations of $MnSb_2Te_4$ nanosheets. **a** Phase-controlled growth schematic of $MnSb_2Te_4$ via the flux-assisted method. **b** Differential scanning calorimeter (DSC) results of the flux and the mixed reactants, showing that the melting points of both are close to 650 °C. **c** Comparison of nine typical fluxes with different melting points based on FTsalt–FACT salt phase diagrams[30]. The blue part indicates deliquescent, moisture-absorbing cosolvents; the cyan part contains salts with melting points above 650 °C that may cause phase separation; and the red region marks salts that tend to alter the MB_2T_4 stoichiometry. **d** Histogram of 156 samples with various Mn: Sb molar ratios at different temperatures to determine proper growth conditions, where 650, 670, 700, 730, and 760 °C are set as the growth temperatures. **e** Diagram of reaction thermodynamics and kinetic competition as a function of temperature. The blue region represents kinetically hindered growth, and the red region indicates thermodynamically hindered conditions. **f** Optical images of $MnSb_2Te_4$ nanosheets on mica. **g** Atomic force microscopy (AFM) image of a ~2.4 nm $MnSb_2Te_4$ nanosheet, with the inset showing the corresponding height profile. **h** Energy dispersive X-ray spectroscopy (EDS) mapping of a ~450 μm region shows elemental distributions of different nanosheets. **i** Histogram of Mn:Sb ratios for 44 samples grown at 700 °C, where ~72.7% are close to the ideal 1:2 stoichiometry.

decompose and remelt. MnTe nanosheets then precipitate from the mixture while the rest part turns into $Mn_{1-x}Sb_2Te_{4-x}$ ($0 \le x \le 1$). More ex-situ EDS images obtained at 500, 650, 680, 700, 730, 760, and 780 °C are shown in Supplementary Fig. 15–21, which indicates the state of the products at each temperature stage in detail.

To further certify the phase separation products of flux-assisted precipitation, AC-TEM is conducted to characterize the final products. Figures 2b, c show the EDS mapping of the phase-separated area, where Sb_2Te_3 samples are grown along the edges of MnTe crystals in a mutually interlocked manner. Figures 2d, e display the high-angle annular dark-field imaging (HAADF) images of Sb_2Te_3 and MnTe, respectively. In the Sb_2Te_3 area, all the atoms show equivalent brightness due to the similar atomic numbers (Z) value of Sb and Te. As a contrast, the strong contrast in Fig. 2e for the MnTe area results from the Z difference of Mn and Te. To assess the universality of the phase control strategy in preparing various 2D MB_2T_4 family materials, $MnSb_4Te_7$, $MnBi_2Te_4$, $MnBi_4Te_7$, $MnBi_2Se_4$, and $MnBi_4Se_7$ bulk crystals are applied as precursors to crystallize into 2D samples with different mixed fluxes. As shown in the inset of Fig. 2f, both $MnBi_2Te_4$ and $MnBi_2Se_4$ display SL structure, while $MnSb_4Te_7$, $MnBi_4Te_7$, and $MnBi_4Se_7$ show alternating QL/SL stacking[33]. Figure 2f also illustrates the crystallization conditions for the listed materials, where 2D $MnBi_2Te_4$ and $MnBi_4Te_7$ can only be obtained under a strict growth condition (~590 °C) with 0.4 mol NaCl and 0.6 mol NaI as flux (melting point of ~575 °C) due to the poor thermal stability[34]. For the rest, NaCl–KCl mixed flux can satisfy their growth conditions.

https://doi.org/10.1038/s41467-026-68426-z

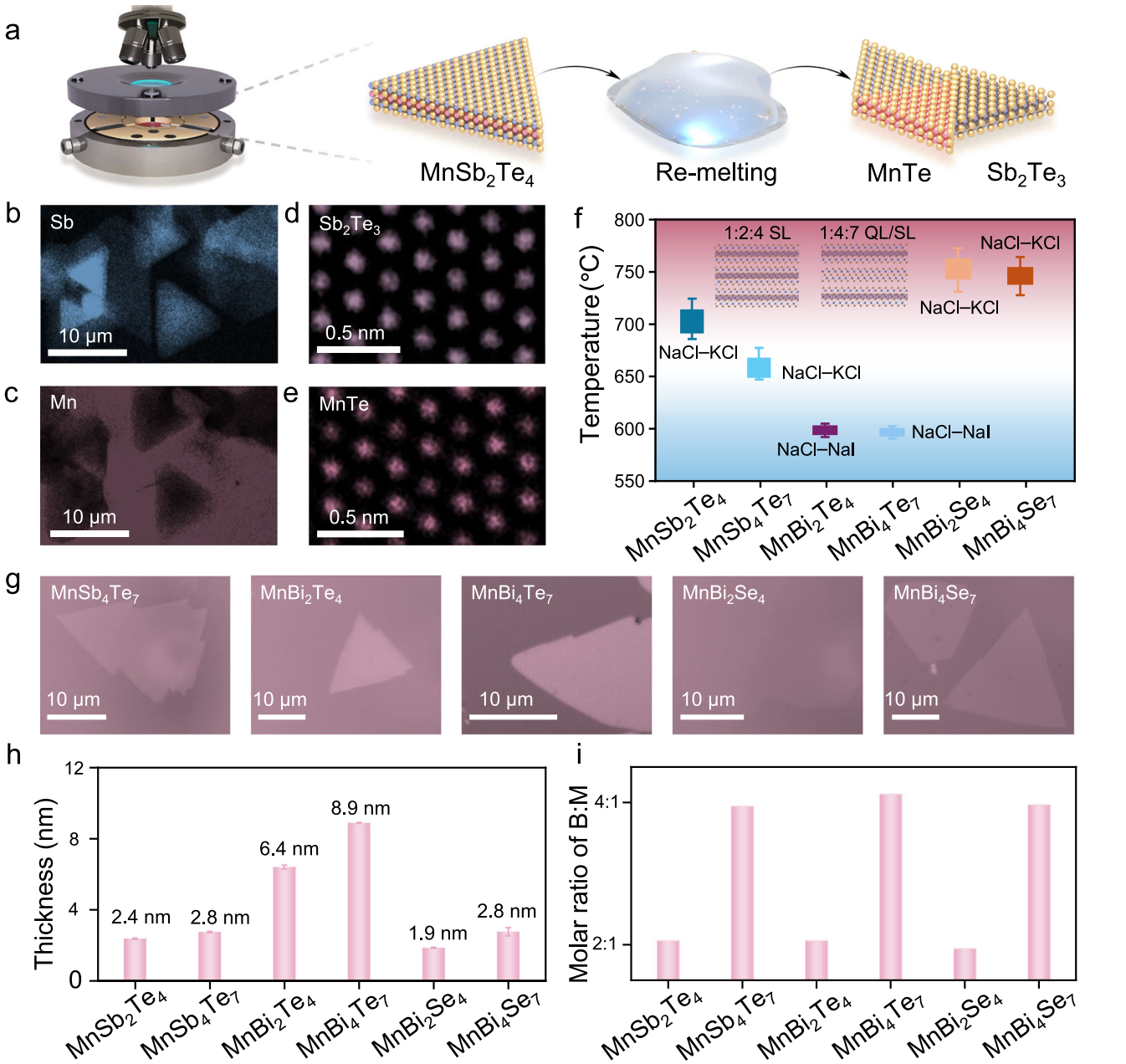

Fig. 2 | In-situ study of the flux-assisted crystallization mechanism. a Schematic illustrations of the in-situ growth process of the target crystals and byproducts at different temperatures. **b**, **c** Sb and Mn EDS mappings of the phase-separated area grown at 760 °C. Obvious Sb_2Te_3 and MnTe samples are grown in a mutually interlocked manner, indicating phase separation. **d**, **e** High-angle annular dark-field imaging (HAADF) of Sb_2Te_3 and MnTe products. **f** The parameters of the flux-assisted method in synthesizing thin-layer MB_2T_4 family materials. The inset crystal structures show the atomic arrangements of MB_2T_4 and MB_4T_7. SL and QL represent septuple and quintuple layers, respectively. The growth conditions include fluxes and temperature for $MnSb_2Te_4$, $MnSb_4Te_7$, $MnBi_2Te_4$, $MnBi_4Te_7$, $MnBi_2Se_4$, and $MnBi_4Se_7$, respectively, where the box area represents their corresponding appropriate temperature while the upper and lower whiskers indicate the maximum and minimum achievable synthesis temperatures, respectively. **g** Optical images of the obtained samples. **h** AFM results of the six 2D MB_2T_4 family materials. Error bars represent the standard deviation obtained from three independent measurements. **i** EDS results of these 2D MB_2T_4 and MB_4T_7 materials show a close stoichiometric ratio to their standard formula.

Although these species can precipitate from the mixed flux over a wide temperature range, the most appropriate growth temperatures for $MnSb_4Te_7$, $MnBi_2Se_4$, and $MnBi_4Se_7$ are quite hard to obtain pure phase products (660, 750, and 730 °C, respectively). The upper and lower whiskers in Fig. 2f indicate the maximum and minimum achievable synthesis temperatures, respectively. The obtained 2D MB_2T_4 family materials illustrate triangular or hexagonal shapes with lateral domain sizes of tens of microns as shown in Fig. 2g. Figure 2h shows the AFM results of the grown 2D MB_2T_4 family materials, where the detected minimum thickness for 2D $MnSb_4Te_7$, $MnBi_2Te_4$, $MnBi_4Te_7$, $MnBi_2Se_4$, and $MnBi_4Se_7$ is ~2.8, 6.4, 8.9, 1.9 and 2.8 nm, respectively. EDS test further confirms the chemical stoichiometric ratio of the grown 2D nanosheets in Fig. 2i, close to the ideal chemical composition. Detailed characterizations using EDS, AFM, Raman, and TEM are shown in Supplementary Figs. 25–27. The successful preparation of 2D MB_2T_4 family crystals proves the feasibility of flux-assisted precipitation for multi-element complex materials.

https://doi.org/10.1038/s41467-026-68426-z

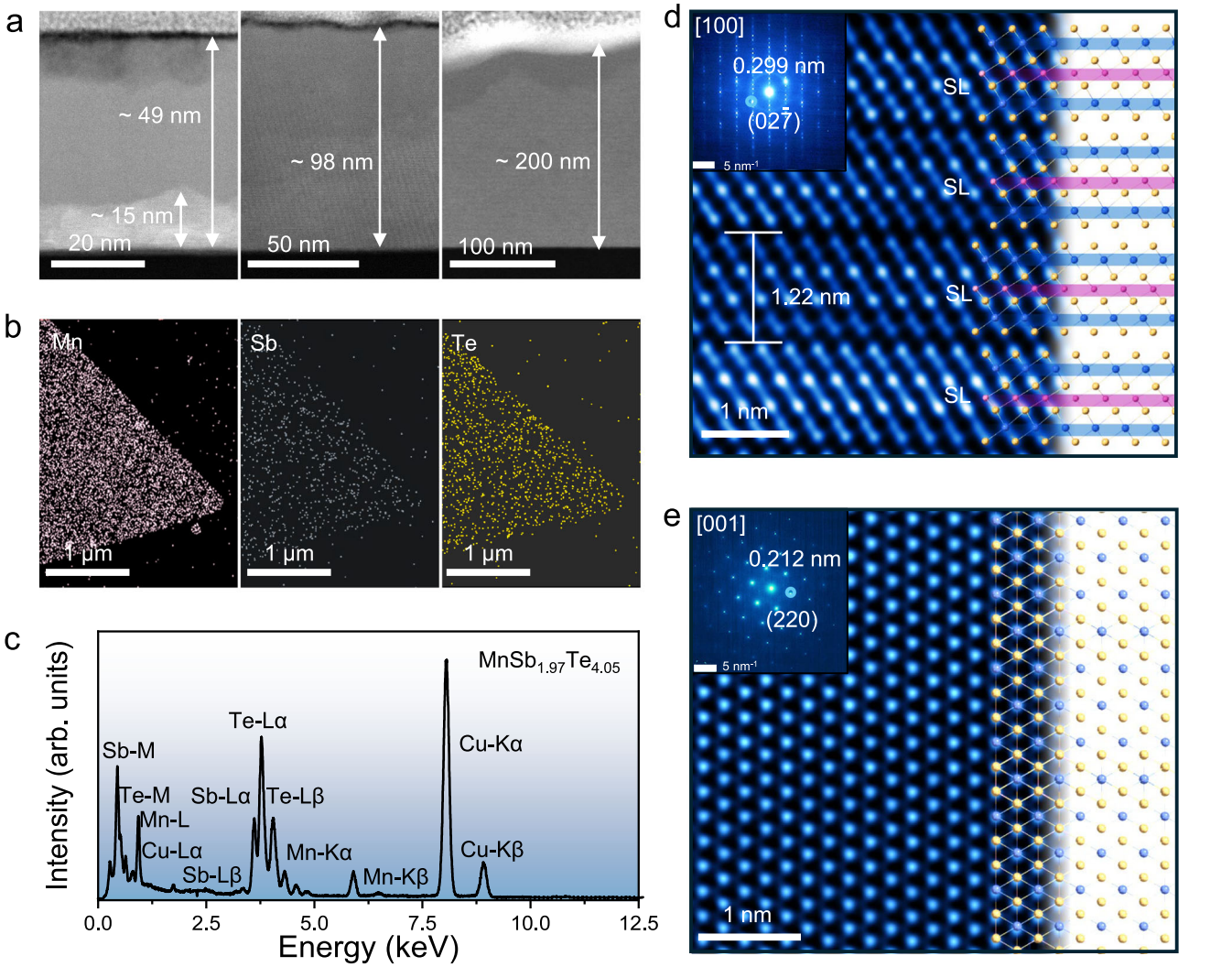

Fig. 3 | Atomic arrangements and crystal structures of the obtained samples. **a** Cross-section aberration-corrected transmission electron microscopy (AC-TEM) of the characterized samples manipulated by the focused ion beam (FIB) with 3 different thicknesses. **b** Fine EDS mapping of the tested area from the ab plane. **c** EDS point scanning result of the obtained samples shows a stoichiometric ratio close to 1:2:4. **d** Cross-section AC-TEM images of $MnSb_2Te_4$ crystals, showing ordered septuple-atom layers. The inset is the corresponding selected area electron diffraction (SAED) results. On the right part, atomic lattice schematic along the [100] direction is embedded and shows excellent agreement with the AC-TEM results. **e** The amplified high-angle annular dark-field images of the atomic images from [001] and their corresponding atomic annotations. The inset is the corresponding SAED result, showing their single-crystal features. The atomic lattice schematic on the right part along the [001] direction is embedded on the right, matching well with the experimental data.

Structural characterization of $MnSb_2Te_4$

AC-TEM is further conducted to analyze the crystal structures and atomic arrangements of the as-grown nanosheets. We selected three samples of different thicknesses for cross-sectional TEM imaging. As shown in Fig. 3a, the low-magnification images display the initial sample thicknesses of approximately 49, 98, and 200 nm, with the samples sandwiched between the substrates and the deposited Pt layer. Due to the poor stability of the material, surface degradation occurred during transfer and FIB preparation, resulting in a smaller effective thickness. The atomic arrangements of the ab plane are also analyzed by AC-TEM. The uniform element distribution of Mn, Sb, and Te on the ab plane with sharp edges in Fig. 3b demonstrates the chemical uniformity. The stoichiometry ratio of the sample is indicated in Fig. 3c, close to 1:2:4, proving the feasibility of component control. Figure 3d presents cross-sectional HAADF images of $MnSb_2Te_4$ nanosheets, in which no staggered layers such as Sb_2Te_3 are observed, demonstrating effective control over phase purity. Complementary cross-sectional AC-TEM analyses for the other 2 thinner samples in Supplementary Fig. 29 consistently reveal a well-ordered SL-type stacking without any indication of QL-type phase separation, indicating that the stacking order remains unaffected by thickness and corroborating the effectiveness of the phase-controlled growth strategy. Figure 3e shows the HAADF images along the *c*-axis, indicating a single-crystal nature. The inset in Figs. 3d, e displays the selected area electron diffraction (SAED) result, where the indexed lattice plane is consistent with the lattice parameters. The atomic structure and corresponding annotations are illustrated in the image, where the pink middle atomic layers represent the Mn layer due to its smaller atomic number. The results of AC-TEM further validate the high quality of the samples, concurrently showcasing the capability of this method in phase control.

Magnetic properties of $MnSb_2Te_4$

SQUID and RMCD are further conducted to study the magnetic properties of the obtained nanosheets. The previous simulation and experiment results illustrate that a transition from paramagnetic to antiferromagnetic occurs below a certain temperature in pure bulk $MnSb_2Te_4$, even though the value of Néel temperature (T_N) is

https://doi.org/10.1038/s41467-026-68426-z

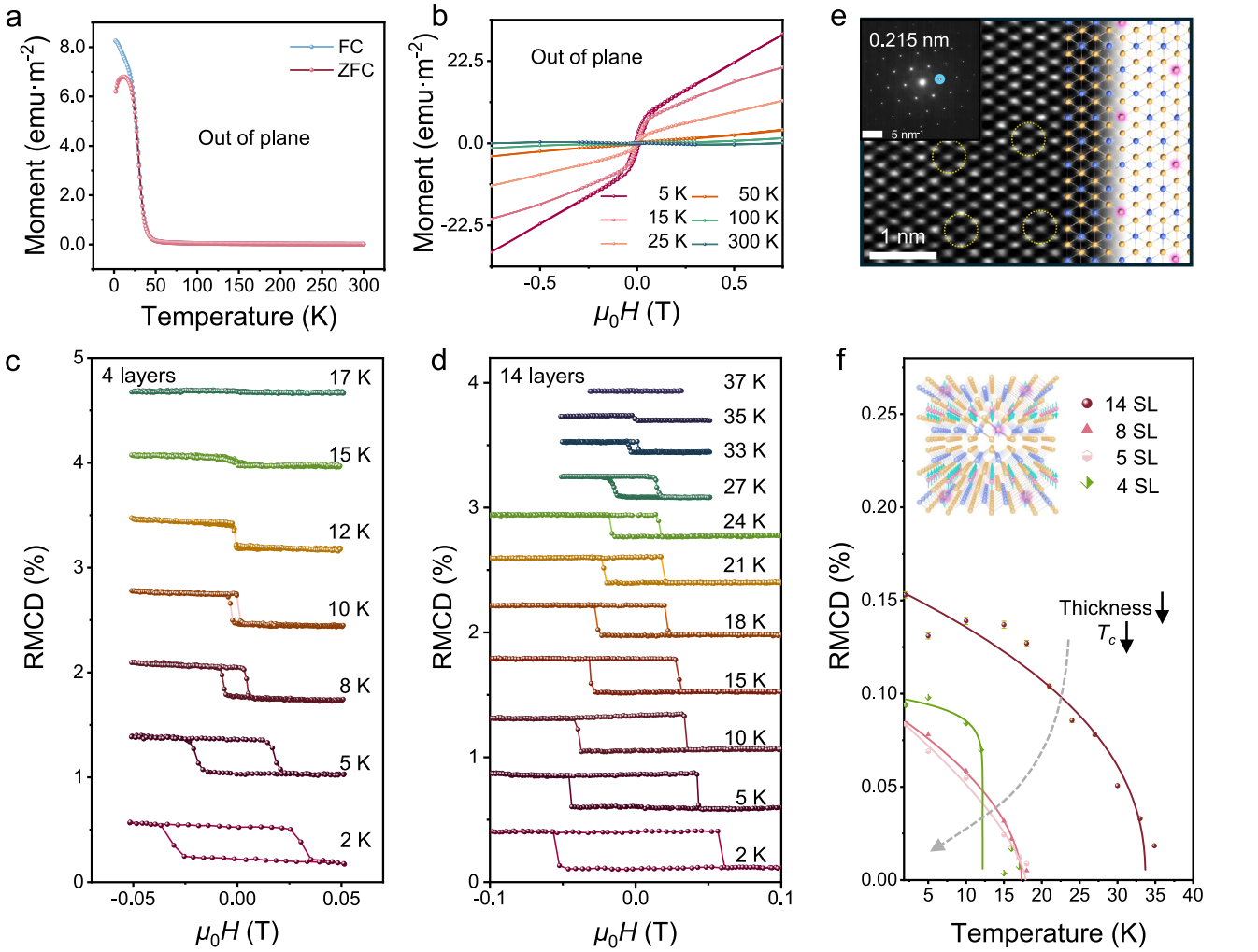

Fig. 4 | Magnetic properties of the obtained $MnSb_2Te_4$ nanosheets. a Out-of-plane magnetization-temperature (M–T) measurement curves of the samples with zero field cooling (ZFC) and field cooling (FC), showing ferromagnetic features with Curie temperature (T_c) ~25 K. **b** Out-of-plane magnetization-magnetic field (M–H) measurement curves at 5, 15, 25, 50, 100, and 300 K, where obvious hysteresis loops appear below 25 K. The data for **a**, **b** are collected from superconducting quantum interference device test (SQUID). μ_0 is the vacuum permeability, H is the magnetic field strength, and μ_0H represents the magnetic field expressed in tesla (T). **c** Reflective magnetic circular dichroism (RMCD) results for $MnSb_2Te_4$ nanoflake of 4.8 nm (~4 layers) at different temperatures, where the hysteresis loop vanishes at 17 K. **d** RMCD results for $MnSb_2Te_4$ nanoflake of 17.3 nm (~14 layers) at different temperatures. **e** HAADF images of the samples with substitutions between Sb and Mn. Yellow circles mark the substituted sites. **f** Remanent RMCD signals of different $MnSb_2Te_4$ samples at zero magnetic field as a function of temperature, showing T_c descends as thickness decreases. Data points represent the remanent RMCD values extracted from hysteresis loops, while the solid lines are fits to the critical scaling function $M = A(1\text{-}T/T_c)^{\beta}$, where M is the magnetization, A is a constant, T is the temperature, T_c is the Curie temperature, and β is the critical exponent. The inset is the illustration of magnetic coupling in the substituted $MnSb_2Te_4$ system.

controversial[21,35]. In a single-layer $MnSb_2Te_4$, Mn atoms provide the out-of-plane non-zero magnetic moments. In multiple-layer samples, spins of Mn in adjacent layers point in opposite directions, showing A-type antiferromagnetic behaviors[26,35]. However, Fig. 4a, b display the out-of-plane magnetization-temperature (M–T) and magnetization-magnetic field (M–H) curves, where the ferromagnetic transition occurs around 25 K, supported by the slope change in the M–T curves at this point. M–H curves at 5, 15, and 25 K display apparent hysteresis loops. When the temperature increases, the loops shrink and finally disappear. Even though the SQUID signals are obtained from many nanosheets, they still provide strong evidence for the judgment of the ferromagnetic properties of the obtained samples. To precisely characterize the magnetic properties of one single nanosheet, RMCD is further conducted on $MnSb_2Te_4$ nanosheets with different thicknesses, as Fig. 4c, d, where RMCD signals at different temperatures are collected. For the sample with a thickness of 4.8 nm (~4 layers) in Fig. 4c, the hysteresis loops start to appear below 17 K and gradually enlarge as the temperature is lowered to 2 K, which is consistent with the traditional ferromagnetic behavior and the SQUID results. As for the 17.3 nm (~14 layers) sample in Fig. 4d, a similar transition occurs at ~33 K. The reason why the obtained nanosheets exhibit ferromagnetism may be the inevitable substitution between Mn and Sb atoms, which has been widely reported in the previous literature[21,23,35–39]. The effects of various kinds of substitution types between Mn and Sb on magnetic properties have been well studied, where the replacement of Sb by Mn–Sb antisites may introduce another magnetic moment in the antiferromagnetic system, making $MnSb_2Te_4$ a ferromagnet below the T_c[40].

Notably, the HAADF images of the ab plane from another sample show that dark dots exist on the periodic background, in which the substitution between Mn and Sb contributes to these atomic impurities in Fig. 4e. Generally, during the preparation process, it only takes several seconds to achieve crystallization from flux; hence, atomic misalignments will be inevitable. The substitution defects are also observed in the samples synthesized by other methods, such as solid-state reaction route, chemical vapor transport method, and molecular

beam epitaxy, induced by rapid cooling and metastable thermodynamics[21,35–37]. Meanwhile, the substitution of Mn with adjacent Sb atoms introduces negligible lattice stress reflected by the similar diffraction data from the insets in Figs. 3e and 4e. Therefore, the small lattice distortion energy further diminishes the driving force for crystal recovery[38]. Besides, Density Functional Theory (DFT) calculations show that Mn–Sb antisite substitution has the lowest formation energy (−0.1492 eV) compared to Sb–Te substitution, demonstrating that such substitution is thermodynamically favorable in Supplementary Fig. 32. Furthermore, the M–T curves of the Chemical Vapor Transport (CVT)-grown bulk samples also exhibit a ferromagnetic signal with T_c ~27 K in Supplementary Fig. 31, which is close to the value above rather than showing antiferromagnetic behavior, thereby providing further evidence that Mn–Sb antisite substitution is present. Hence, we attribute the origin of magnetism to the atomic misalignment. Other RMCD data from the samples with different thicknesses are illustrated in Supplementary Fig. 33. T_c from these samples with different thicknesses by RMCD is statistically analyzed in Fig. 4f, where the remnant RMCD signals are extracted from hysteresis loops and fitted by the functional form $A(1-T/T_c)^{\beta}$ (A, T_c, and β are simultaneous parameters). It is obvious that the detected T_c falls from 33.7 to 12.3 K as the thickness of the samples decreases, similar to the regularity in plenty of 2D magnets such as Fe_3GeTe_2. This is because the weakening of interlayer exchange interactions with thickness drops, making it hard to resist thermal fluctuations[41–44]. However, as shown in Supplementary Fig. 34, $MnSb_2Te_4$ exhibits a non-monotonic coercivity (H_c)-thickness trend at 2 K, in contrast to conventional 2D ferromagnets such as Fe_3GeTe_2 and $Cr_2Ge_2Te_6$, where H_c typically increases monotonically with decreasing thickness owing to enhanced magnetic anisotropy[41,45]. In $MnSb_2Te_4$, although reduced dimensionality is also expected to enhance anisotropy, ferromagnetism is largely mediated by Mn–Sb antisite defects. The density of such defects may decrease in thinner flakes, weakening FM exchange interactions and lowering the magnetic moment density. In addition, ultrathin flakes are more susceptible to surface and edge disorder as well as degradation, which destabilize magnetic domains and suppress anisotropy[26,41,45–48]. The competition among these effects gives rise to a maximum H_c at intermediate thickness, a trend consistent with previous observations in mechanically exfoliated $MnSb_2Te_4$.

In summary, we developed a universal flux-assisted phase-controlled strategy with proper mixed salts as a flux to successfully obtain 6 kinds of ultrathin MB_2T_4 family crystals. Besides, the phase-separation mechanism has been thoroughly investigated via in-situ and ex-situ methods, making the thermodynamic and kinetic control of phase and thickness in 2D materials effective. The strategy may be inspiring for the controlled synthesis of other complex and multi-element 2D compounds. Additionally, in the ultrathin $MnSb_2Te_4$ nanosheets, it is found that the substitution of Mn atoms and Sb atoms can introduce ferromagnetic behavior with tunable T_c from ~12.3 to 33.7 K as the thickness increases, paving a promising way to study fundamental physics and design exotic dissipationless nanodevices.

Methods

Synthesis of bulk MB_2T_4 crystals

Bulk MB_2T_4 crystals were synthesized via a carefully controlled CVT method. $MnSb_2Te_4$ is described here as a representative example. High-purity elemental precursors, including manganese, antimony, and tellurium were weighed in a stoichiometric ratio of 1:2:4. The mixture was sealed in a quartz ampoule under high vacuum (~10^{-5} Torr) to prevent oxidation. To ensure complete precursor mixing and suppress the formation of secondary phases in cooler regions, the sealed ampoule was fully positioned within the high-temperature zone of tube furnace. The thermal process included several key stages: First, the temperature was rapidly ramped to 900 °C in 1 h and maintained for 2 h. Then, the system was cooled to 647 °C over 0.5 hours, establishing conditions suitable for controlled nucleation and crystal growth. The tube was then held at 647 °C for 48 h to facilitate crystal growth. Finally, the furnace was cooled to room temperature over 2 h, yielding bulk $MnSb_2Te_4$ crystals. Other MB_2T_4-family crystals were synthesized following the same CVT procedure, with appropriate adjustments to precursor stoichiometry and growth temperature, as summarized below: For $MnSb_4Te_7$ crystals, Mn, Sb, and Te were weighed with a molar ratio of 1:4:7. The system was first heated to 900 °C in 1 h and then cooled from 900 °C to 628 °C over 0.5 h and held at 628 °C for 48 h. For $MnBi_2Te_4$ crystals, Mn, Bi, and Te were weighed with a molar ratio of 1:2:4. The system was first heated to 900 °C and held for 2 h, then cooled from 900 °C to 590 °C over 40 min and held at 590 °C for 72 h. For $MnBi_4Te_7$ crystals, Mn, Bi, and Te were weighed with a molar ratio of 1:4:7. The system was first heated to 900 °C and held for 2 h, then cooled from 900 °C to 580 °C over 45 min and held at 580 °C for 72 h. For $MnBi_2Se_4$ crystals, Mn, Bi, and Se were weighed with a molar ratio of 1:2:4. The furnace temperature was ramped to 750 °C within 45 min and maintained for 48 h. For $MnBi_4Se_7$ crystals, Mn, Bi, and Se were weighed with a molar ratio of 1:4:7. The furnace temperature was ramped to 725 °C within 40 min and maintained for 48 h. After the growth stage, all samples were cooled to room temperature before removal from the furnace.

Synthesis of 2D MB_2T_4 crystals

All 2D MB_2T_4-family nanosheets were synthesized using a flux-assisted growth method starting from bulk MB_2T_4 precursors. 2D $MnSb_2Te_4$ is described below as an example. For the growth of $MnSb_2Te_4$ nanosheets, ~2 mg of bulk $MnSb_2Te_4$ crystal powder was mixed with ~4 mg of a NaCl–KCl cosolvent with an equimolar composition. The mixture was finely ground to ensure homogeneous mixing. Then the powders were uniformly spread between two freshly cleaved mica substrates, forming a mica-precursor-mica sandwich configuration. Next, the mica was placed between the self-designed equipment made of stainless steel and compressed tightly by tightening the screws. Then, the equipment was heated to 700 °C in 25 min and maintained for 3 min with 100 sccm Ar as protective gas. Finally, the samples can be taken out after the furnace and equipment cool down naturally. Other MB_2T_4 family nanosheets were synthesized following the same flux-assisted procedure, with appropriate adjustments to the salt composition, growth temperature, and gas atmosphere, as summarized below:

For 2D $MnSb_4Te_7$, ~2 mg $MnSb_4Te_7$ bulk powder mixed with ~4 mg of equimolar NaCl–KCl salts. The assembly was heated to 660 °C within 20 min and held for 3 min under 100 sccm Ar.

For 2D $MnBi_2Te_4$, ~2 mg $MnBi_2Te_4$ bulk crystals mixed with ~4 mg of NaCl–NaI mixed salt with a NaCl:NaI molar ratio of 2:3. The assembly was heated to 590 °C within 20 min and held for 3 min under a mixed 100 sccm Ar/H_2 atmosphere.

For 2D $MnBi_4Te_7$, ~2 mg $MnBi_4Te_7$ bulk powders mixed with ~4 mg of a NaCl–NaI mixed salt (NaCl:NaI = 2:3). The assembly was heated to 585 °C within 20 min and held for 3 min under 100 sccm Ar/H_2 mixed gas.

For 2D $MnBi_2Se_4$, ~2 mg $MnBi_2Se_4$ bulk powders mixed with ~4 mg of an equimolar NaCl–KCl salt. The assembly was heated to 750 °C within 25 min and held for 3 min under 100 sccm Ar.

For 2D $MnBi_4Se_7$, ~2 mg $MnBi_4Se_7$ bulk crystals mixed with ~4 mg of an equimolar NaCl–KCl salt. The assembly was heated to 730 °C within 25 min and held for 3 min under 100 sccm Ar.

AC-TEM characterization

Crystal structures were analyzed by AC-TEM, among which the samples tested along the c-axis were prepared by poly(methyl methacrylate) (PMMA) (950 PMMA A4, Micro Chem)-assisted method. First, the samples were spin-coated with PMMA and then etched with 3% hydrofluoric acid. Afterward, the peeled-off PMMA/sample was washed with deionized water and then transferred onto the copper

TEM grids. Lastly, PMMA was removed by acetone. As for the preparation of cross-section samples, $MnSb_2Te_4$ nanosheets were first transferred onto SiO_2/Si substrates by the PMMA-assisted method. After that, the picked $MnSb_2Te_4$ crystal was plated with a ~100 nm Pt layer and then cut along the predetermined direction to expose the cross-section crystal plane by FIB (Helios G4). Both *c*-axis oriented and cross-sectional AC-TEM measurements were carried out using a FEI Themis Z microscope operated at an accelerating voltage of 300 kV.

RMCD measurement

The RMCD measurements were performed using the Attocube closed-cycle cryostat (attoDRY2100), with temperatures down to 2 K and out-of-plane magnetic fields up to 9 T. The linearly polarized light of the 633-nm He–Ne laser was modulated between left and right circular polarization by a photoelastic modulator (PEM) and focused onto the sample through a high numerical aperture (NA = 0.82) objective. The reflected light was detected by a photomultiplier tube (THORLABS PMT1001/M). The magnetic reversal under the external magnetic field was detected by the RMCD signal determined by the ratio of the a.c. component of PEM at 50.05 kHz and the a.c. component of the chopper at 779 Hz, measured using a two-channel lock-in amplifier (Zurich HF2LI).

Data availability

The Source Data underlying the figures of this study are available at https://doi.org/10.6084/m9.figshare.29949827. All raw data generated during the current study are available from the corresponding authors upon request.

References

1. Rienks, E. D. L. et al. Large magnetic gap at the Dirac point in Bi_2Te_3/$MnBi_2Te_4$ heterostructures. *Nature* **576**, 423–428 (2019).
2. Otrokov, M. M. et al. Prediction and observation of an antiferromagnetic topological insulator. *Nature* **576**, 416–422 (2019).
3. Otrokov, M. M. et al. Unique thickness-dependent properties of the van der Waals interlayer antiferromagnet $MnBi_2Te_4$ films. *Phys. Rev. Lett.* **122**, 107202 (2019).
4. Wu, J. et al. Natural van der Waals heterostructural single crystals with both magnetic and topological properties. *Sci. Adv.* **5**, eaax9989 (2019).
5. Hao, Y. J. et al. Gapless surface Dirac cone in antiferromagnetic topological insulator $MnBi_2Te_4$. *Phys. Rev. X.* **9**, 041038 (2019).
6. Chen, B. et al. Intrinsic magnetic topological insulator phases in the Sb-doped $MnBi_2Te_4$ bulks and thin flakes. *Nat. Commun.* **10**, 4469 (2019).
7. Liu, C. et al. Robust axion insulator and Chern insulator phases in a two-dimensional antiferromagnetic topological insulator. *Nat. Mater.* **19**, 522–527 (2019).
8. Hu, C. et al. A van der Waals antiferromagnetic topological insulator with weak interlayer magnetic coupling. *Nat. Commun.* **11**, 97 (2020).
9. Ge, J. et al. High-Chern-number and high-temperature quantum Hall effect without Landau levels. *Natl. Sci. Rev.* **7**, 1280–1287 (2020).
10. Lujan, D. et al. Magnons and magnetic fluctuations in atomically thin $MnBi_2Te_4$. *Nat. Commun.* **13**, 2527 (2022).
11. Zhu, T. et al. Synthesis, magnetic properties, and electronic structure of magnetic topological insulator $MnBi_2Se_4$. *Nano Lett.* **21**, 5083–5090 (2021).
12. Gong, Y. et al. Experimental realization of an intrinsic magnetic topological insulator. *Chin. Phys. Lett.* **36**, 076801 (2019).
13. Li, J. et al. Intrinsic magnetic topological insulators in van der Waals layered $MnBi_2Te_4$-family materials. *Sci. Adv.* **5**, eaaw5685 (2019).
14. Aliev, Z. S. et al. Novel ternary layered manganese bismuth tellurides of the MnTe–Bi_2Te_3 system: Synthesis and crystal structure. *J. Alloys Compd.* **789**, 443–450 (2019).
15. Zhang, Z. et al. Controlled large non-reciprocal charge transport in an intrinsic magnetic topological insulator $MnBi_2Te_4$. *Nat. Commun.* **13**, 6191 (2022).
16. Padmanabhan, H. et al. Interlayer magnetophononic coupling in $MnBi_2Te_4$. *Nat. Commun.* **13**, 1929 (2022).
17. Klimovskikh, I. I. et al. Tunable 3D/2D magnetism in the $(MnBi_2Te_4)(Bi_2Te_3)_m$ topological insulators family. *npj Quantum Mater.* **5**, 54 (2020).
18. Orujlu, E. N. et al. Phase equilibria of the MnTe–Sb_2Te_3 system and synthesis of novel ternary layered compound $MnSb_4Te_7$. *J. Phys. Chem. Solids* **22**, 39–44 (2021).
19. Yan, J. Q. et al. Crystal growth and magnetic structure of $MnBi_2Te_4$. *Phys. Rev. Mater.* **3**, 064202 (2019).
20. Zeugner, A. et al. Chemical aspects of the candidate antiferromagnetic topological insulator $MnBi_2Te_4$. *Chem. Mater.* **31**, 2795–2806 (2019).
21. Wimmer, S. et al. Mn-Rich $MnSb_2Te_4$: a topological insulator with magnetic gap closing at high Curie temperatures of 45–50 K. *Adv. Mater.* **33**, e2102935 (2021).
22. Li, H. et al. Antiferromagnetic topological insulator $MnBi_2Te_4$: synthesis and magnetic properties. *Phys. Chem. Chem. Phys.* **22**, 556–563 (2020).
23. Lai, Y. et al. Defect-driven ferrimagnetism and hidden magnetization in $MnBi_2Te_4$. *Phys. Rev. B* **103**, 184429 (2021).
24. Yang, S. et al. Odd-even layer-number effect and layer-dependent magnetic phase diagrams in $MnBi_2Te_4$. *Phys. Rev. X* **11**, 011003 (2021).
25. Chen, P. et al. Tailoring the magnetic exchange interaction in $MnBi_2Te_4$ superlattices via the intercalation of ferromagnetic layers. *Nat. Electron.* **6**, 18–27 (2023).
26. Zang, Z. H. et al. Layer-number-dependent antiferromagnetic and ferromagnetic behavior in $MnSb_2Te_4$. *Phys. Rev. Lett.* **128**, 017201 (2022).
27. Huang, Y. et al. Universal mechanical exfoliation of large-area 2D crystals. *Nat. Commun.* **11**, 2453 (2020).
28. Deng, Y. et al. Quantum anomalous Hall effect in intrinsic magnetic topological insulator $MnBi_2Te_4$. *Science* **367**, 895–900 (2020).
29. Guo, H. et al. Controllable synthesis of high-quality magnetic topological insulator $MnBi_2Te_4$ and $MnBi_4Te_7$ multilayers by chemical vapor deposition. *Nano Lett.* **24**, 15788–15795 (2024).
30. Broström, M. et al. Condensation in the KCl–NaCl system. *Fuel Process. Technol.* **105**, 142–148 (2013).
31. Zhang, P. et al. Flux-assisted growth of atomically thin materials. *Nat. Synth.* **1**, 864–872 (2022).
32. Orujlu, E. N. Phase relations and characterization of solid solutions in the $SnSb_2Te_4$–$MnSb_2Te_4$ system. *New Mater. Compd. Appl.* **4**, 38–43 (2020).
33. Li, P. et al. Electronic structure and topological phases of the magnetic layered materials $MnBi_2Te_4$, $MnBi_2Se_4$, and $MnSb_2Te_4$. *Phys. Rev. B* **103**, 155118 (2021).
34. Orujlu, E. N. Phase equilibria in the $SnBi_2Te_4$–$MnBi_2Te_4$ system and characterization of the $Sn_{1-x}Mn_xBi_2Te_4$ solid solutions. *Phys. Chem. Solid State* **21**, 113–116 (2020).
35. Yan, D. Y. et al. Site mixing induced ferrimagnetism and anomalous transport properties of the Weyl semimetal candidate $MnSb_2Te_4$. *Phys. Rev. B* **103**, 224412 (2021).
36. Liu, Y. H. & Yan, J. Q. Site Mixing and complex magnetic structures in topological insulators $MnBi_2Te_4$ and $MnSb_2Te_4$. *Acta Crystallogr. A* **78**, A105–A105 (2022).
37. Folkers, L. C. et al. Occupancy disorder in the magnetic topological insulator candidate $Mn_{1-x}Sb_{2+x}Te_4$. *Z. Kristallogr. Cryst. Mater.* **237**, 101–108 (2022).

38. Yang, W., Han, Z. & Zheng, G. The influences of lattice distortion on the antiferroelectric transition and relaxation of oxygen vacancies in high-entropy perovskites ($Bi_{0.2}Na_{0.2}Ba_{0.2}K_{0.2}X_{0.2}$) TiO_3 with X=Ca, Sr or La. *Scr. Mater.* **203**, 114096 (2021).
39. Li, H. et al. Glassy magnetic ground state in layered compound $MnSb_2Te_4$. *Sci. China Mater.* **65**, 477–485 (2022).
40. Bac, S. K. et al. Topological response of the anomalous Hall effect in $MnBi_2Te_4$ due to magnetic canting. *npj Quantum Mater.* **7**, 46 (2022).
41. Tan, C. et al. Hard magnetic properties in nanoflake van der Waals Fe_3GeTe_2. *Nat. Commun.* **9**, 1554 (2018).
42. Fei, Z. et al. Two-dimensional itinerant ferromagnetism in atomically thin Fe_3GeTe_2. *Nat. Mater.* **17**, 778–782 (2018).
43. Gong, C. et al. Discovery of intrinsic ferromagnetism in two-dimensional van der Waals crystals. *Nature* **546**, 265–269 (2017).
44. Wang, N. et al. Transition from ferromagnetic semiconductor to ferromagnetic metal with enhanced Curie temperature in $Cr_2Ge_2Te_6$ via organic ion intercalation. *J. Am. Chem. Soc.* **141**, 17166–17173 (2019).
45. Mogi, M. et al. Ferromagnetic insulator $Cr_2Ge_2Te_6$ thin films with perpendicular remanence. *APL Mater.* **6**, 091104 (2018).
46. Victora, R. H. Predicted time dependence of the switching field for magnetic materials. *Phys. Rev. Lett.* **63**, 457–460 (1989).
47. Xiong, J. et al. High concentration intrinsic defects in $MnSb_2Te_4$. *Materials* **16**, 5496 (2023).
48. Xi, M. et al. Relationship between antisite defects, magnetism, and band topology in $MnSb_2Te_4$ crystals with $T_c \approx 40$ K. *J. Phys. Chem. Lett.* **13**, 10897–10904 (2022).

Acknowledgements

Y.G. thanks the National Key Basic Research and Development program of China (2024YFA1409100), the National Natural Science Foundation of China (92477112, 22171016), the Fundamental Research Funds for the Central Universities, and the 111 Project (B17002). P.Z. acknowledges the National Natural Science Foundation of China (52302161). Z.L. thanks the National Research Foundation-Competitive Research Program (NRF-CRP22-2019-0007), the Singapore Ministry of Education Tier 3 Programme "Geometrical Quantum Materials" AcRF Tier 3 (MOE2018-T3-1-002), and the Ministry of Education, Singapore, under its Research Centre of Excellence award to the Institute for Functional Intelligent Materials (No. EDUNC-33-18-279-V12). B.T. thanks the Ministry of Education, Singapore, under grant AcRF TIER 2 (MOE T2EP50221-0003).

Author contributions

X.W. and S.Y. contributed equally to this work. X.W. focused on growth control, composition, structural characterization, and overall manuscript preparation, while S.Y. concentrated on magnetic characterization, data interpretation, and drafting of related sections. X.H. processed RMCD data and performed sample testing, with Y.Y. providing guidance on magnetic property analysis and interpretation. J.W. and K.S. collected and processed SQUID data, respectively. H.J. carried out spectroscopic measurements and analysis. Q.H. performed TEM data collection and analysis. B.L. conducted DFT simulations. B.K.T. guided manuscript organization. Z.L. refined and revised the manuscript. P.Z. and Y.G. supervised the overall study design and manuscript preparation. All authors contributed to discussions and the final manuscript.

Competing interests

The authors declare no competing interests.

Additional information

Supplementary information The online version contains supplementary material available at https://doi.org/10.1038/s41467-026-68426-z.

Correspondence and requests for materials should be addressed to Peng Zhang, Zheng Liu or Yongji Gong.

Peer review information *Nature Communications* thanks Changgu Lee, Seok Joon Yun, and Jinsong Zhang for their contribution to the peer review of this work. A peer review file is available.